Chiral Perovskite Nanoplatelets with Tunable Circularly Polarized Luminescence in the Strong Confinement Regime

Qinxuan Cao,[1‡] Ruyi Song,[2‡] Christopher C. S. Chan,[4] Zhiyu Wang,[1] Pui Ying Wong,[1] Kam Sing Wong,[4] Volker Blum,[*2,3] Haipeng Lu[*1]

[1] Department of Chemistry and Energy Institute, The Hong Kong University of Science and Technology, Clear Water Bay, Kowloon, Hong Kong (SAR), China

[2] Department of Chemistry, Duke University, Durham, North Carolina 27708, United States

[3] Thomas Lord Department of Mechanical Engineering and Material Science, Duke University, Durham, North Carolina 27708, United States

[4] Department of Physics, The Hong Kong University of Science and Technology, Clear Water Bay, Kowloon 999077, Hong Kong (SAR), China

Corresponding Author

Volker Blum[*]: volker.blum@duke.edu

Haipeng Lu[*]: haipenglu@ust.hk

[‡] These two authors contributed equally.

Abstract

Chiral perovskite nanocrystals have emerged as an interesting chiral excitonic platform that combines both structural flexibility and superior optoelectronic properties. Despite several recent demonstrations of optical activity in various chiral perovskite nanocrystals, efficient circularly polarized luminescence (CPL) with tunable energies remains a challenge. The chirality imprinting mechanism as a function of perovskite nanocrystal dimensionality remains elusive. Here, we synthesize atomically thin inorganic perovskite nanoplatelets (NPLs) with precise control of layer thickness and functionalize them by chiral surface ligands, serving as a unique platform to probe the chirality transfer mechanism at the organic/perovskite interface. We find that chirality is successfully imprinted into mono-, bi-, and tri-layer inorganic perovskite NPLs, exhibiting tunable circular dichroism (CD) and CPL responses. However, chirality transfer decreases in thicker NPLs, resulting in decreased CD and CPL dissymmetry factors for thicker NPLs. Aided by large-scale first-principles calculations, we propose that chirality transfer is mainly mediated through a surface distortion rather than a hybridization of electronic states, giving rise to symmetry breaking in the perovskite lattice and spin-split conduction bands. The findings described here provide an in-depth understanding of chirality transfer and design principles for distorted-surface perovskites for chiral photonic applications.

Introduction

Chiral excitonic nanomaterials imprint the chirality into the ground-state and excited-state excitonic transitions, giving rise to unequal absorption and emission of circularly polarized light, which are of practical interest for chiral photonics, catalysis, spintronics, and information technologies[1, 2, 3]. Such chirality imprinting in nanostructures is generally achieved by surface chiral organic ligands or chiral self-assembly strategies. While the majority of chiral excitonic nanomaterials is currently developed in group II-VI semiconductor nanocrystals (NCs)[4-6], chiral metal halide perovskite (MHP) NCs have emerged as a promising platform due to their high photoluminescence quantum yield (PLQY), large spin-orbit coupling, and rich chemical and structural versatility. Several recent reports have shown successful chirality imprinting in colloidal MHP NCs by various chiral ligands[7-10]; however, it remains rare and challenging to achieve tunable circularly polarized luminescence (CPL) based on inorganic chiral perovskite nanostructures. Inorganic chiral perovskite NCs in the strong quantum confinement regime are undeveloped. In addition, the mechanism of chirality transfer from surface ligands to perovskite nanocrystals remains elusive.

Since Gun'ko's first report on chiral luminescent CdS NCs[5], tremendous effort and progress have been made in understanding the chirality transfer mechanism from chiral organic ligands to individual NCs. Two dominant mechanisms are generally proposed in chiral II-VI semiconductor NCs. The first mechanism involves mostly the electronic interactions between the inorganic core and chiral ligands either through the dipolar interactions[11] or orbital hybridization[4] between these two phases. The second chirality transfer mechanism suggests that the surface distortion induced by chiral ligands twists the inorganic NC lattice, resulting in asymmetric chiral NCs or a twisted chiral NC surface. Compared to the conventional II-VI NCs which are inherently more covalent and structural rigid, chiral MHP NCs might possess a different chirality transfer mechanism as they are more structurally soft with large ionic bonding character. However, such a chirality transfer mechanism in MHP NCs remains inclusive, which impedes the rational design of chiral MHP NCs with high chiroptical activity. For instance, Waldeck's work on chiral perovskite NCs proposed a direct chirality imprinting mechanism into the excitonic states of perovskite NCs through electronic interactions[10]. Zhang's recent work suggested that orbital hybridization between chiral organic ligands and perovskite NCs accounts for the observed chirality transfer[7]. However, reports from Yan[8], Duan[3], and Beard[2] independently suggested that chirality transfer mainly arises from a surface structural distortion induced by chiral surface ligands[3] in the perovskite NCs. Thus, a unified picture for the chirality transfer mechanism is still lacking at the perovskite/organic interface.

At the same time, theoretical and computational methods based on first-principles density functional theory (DFT) are also being developed to understand the chirality transfer mechanisms[12] . However, most of the reported chiral semiconductor NCs represent challenging computational problems as they consist of at least several hundreds of atoms and precise crystal structures of nanocrystals do not exist[13]. As such, many computational studies are necessarily based on simplified models and fail to provide an exhaustive search for the most favorable surface chiral organic conformation, crucial for a detailed understanding of their electronic and structural interactions with the inorganic NC core.

We envision that a systematic control of the dimensionality of quantum-confined perovskite NCs will allow one to probe the chirality transfer mechanism by tuning both structural distortion and electronic interactions in the quantum confinement regime. We first synthesize atomically thin colloidal lead bromide nanoplatelets (NPLs) with different layer thicknesses (1–3 monolayers (MLs)), which display tunable bandgap, absorption, and photoluminescence (PL) due to the quantum confinement effect. A subsequent chiral ligand exchange reaction based on *R*-or *S*-β-methylphenethylamine (*R*-or *S*-MPEA) affords chiral perovskite NPLs with tunable circular dichroism (CD) and circularly polarized luminescence (CPL). These chiral perovskite NPLs with tunable bandgaps and chiroptical activity thus serve as an ideal platform to study the chirality transfer mechanisms. Spectroscopic studies show that chirality is successfully imprinted into different perovskite NPLs; however, chirality transfer diminishes in thicker NPLs, which leads to decreased CD and CPL dissymmetry factors in thicker NPL. A large scale, first-principles DFT calculations through exhaustive enumeration of more than 8,000 possible organic conformations at the nanoplatelet surfaces suggests that direct electronic interactions through hybridized organic-inorganic orbitals do not occur near the band edges and strongly support the lattice symmetry breaking induced by organic ligands as the dominate source for band spin-splitting in these chiral perovskite NPLs. Our study provides a CPL manipulation strategy and an in-depth understanding of the interfacial chirality transfer in MHP NPLs from combined experimental and computational efforts.

Results and discussion

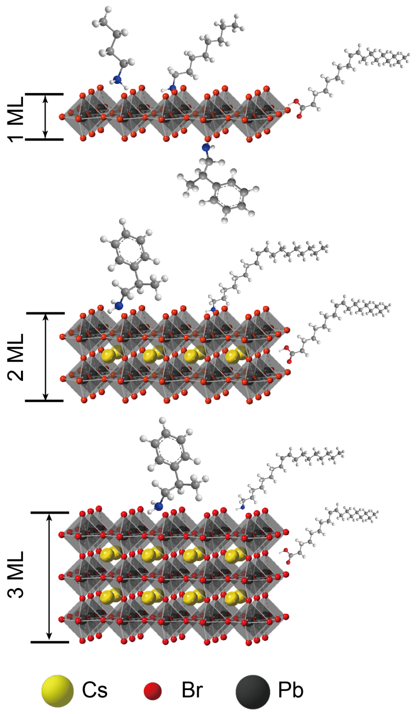

Figure 1. Schematic illustrations of chiral 1 ML, 2 ML and 3 ML $CsPbBr_3$ NPLs.

ssAtomically thin achiral 2D lead bromide perovskite nanoplatelets (NPLs) are first synthesized by a modified room-temperature ligand assisted re-precipitation (LARP) method (see Methods)[8, 14]. By tuning the molar ratio of CsBr to $PbBr_2$, precursor concentration, and reaction time, the layer thickness (n = 1–3 MLs) can be precisely controlled (**Figure 1**).

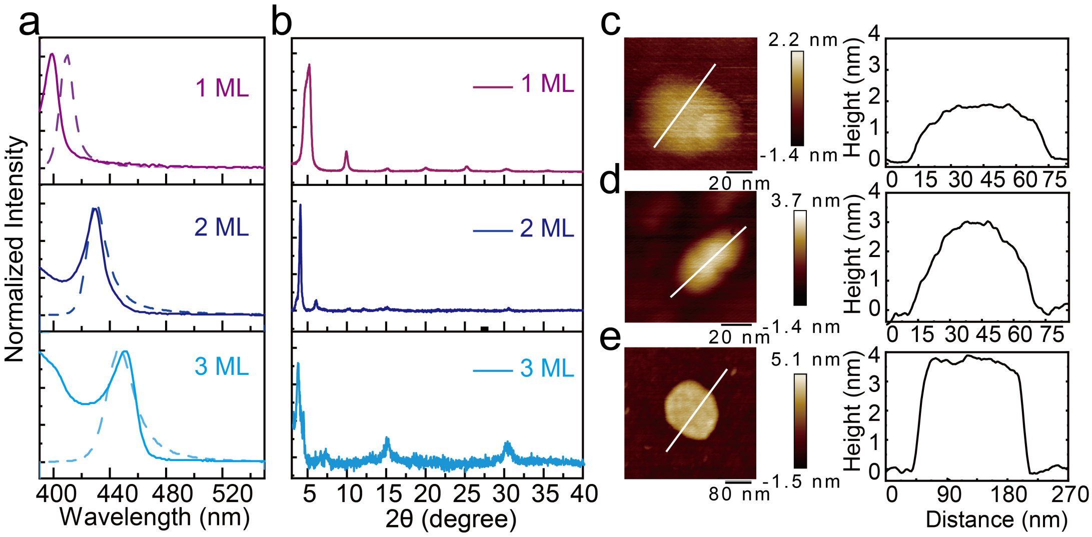

Figure 2. (a) Absorption (solid line) and PL spectra (dashed line) of as-synthesized achiral MHP NPLs with 1, 2 and 3 MLs. (b) XRD pattern of 1, 2 and 3 ML achiral MHP NPLs; (c-e) AFM images of achiral 1, 2 and 3 ML MHP NPLs (left) and corresponding thickness profiles (right).

Due to the quantum confinement effect, thinner perovskite NPLs display larger bandgaps. The thickness of perovskite NPLs can thus be directly probed by their optical bandgaps. **Figure 2a** shows the UV-vis absorption and PL spectra of different perovskite NPLs. The sharp first exciton peak shifts from 400 to 430 and 452 nm, indicating the formation of $CsPbBr_3$ perovskite NPLs with 1, 2, 3 ML thickness, respectively [15,16].Their corresponding PL peaks shift from 409, to 431, and 450 nm. The uniformity in thickness is indicated by the single exciton peak and narrow full width at half maximum (FWHM) of PL peaks. Interestingly, we observed a decreased Stokes shift with increasing perovskite NPL thickness. Similar size-dependent Stokes shifts were previously observed in perovskite nanocrystals,[17] where smaller nanocrystals exhibit larger Stokes shifts compared to larger nanocrystals. This effect was ascribed to an inherent, size-dependent, confined hole state above the valence band edge state, which shifts toward the valence band edge as the nanocrystal size increases. This state is relatively dark in absorption but bright in emission. Therefore, the thinnest nanoplatelets with strongest confinement exhibit the largest Stokes shift.

The phase purity of achiral perovskite NPLs is further characterized by powder X-ray diffraction (PXRD). PXRD patterns of 1, 2, 3 ML $CsPbBr_3$ NPLs all display a primary peak below 6° (**Figure 2b**) corresponding to the (002) plane, which indicates a preferred 2D orientation. The (002) peak shifts to lower angles from 5.2°, to 4°, and 3.5°, indicating an increased d_{002} spacing of 1.7, 2.2, and 2.5 nm for 1, 2, 3 ML $CsPbBr_3$ NPLs, respectively. The perovskite structure can be confirmed by characteristic Bragg diffraction peaks at 15.1° and 30.6°, which are more prominent in thicker NPls (i.e., 3 ML NPLs). Our PXRD patterns of perovskite NPLs are consistent with previous literature reports[8, 14]. The morphology of perovskite NPLs is further probed by atomic force microscopy (AFM) and transmission electron microscopy (TEM). As shown in the height profile (**Figure 2c-e**) and thickness distribution (**Figure S1**), the average thickness is determined as 2.0, 3.0, and 3.6 nm for 1, 2, 3 ML $CsPbBr_3$ NPLs, respectively. Considering the achiral amine attached in 2 and 3 ML $CsPbBr_3$ NPLs (oleyl amine, OAm) is longer than that in 1 ML NPLs (octylamine and butylamine), the increment is nearly one $[PbBr_6]$ octahedron (0.6 nm). Therefore, these results show the layer-by-layer transformation in the vertical direction of perovskite NPLs. TEM images (**Figure S2**) indicate the round shape of 1 ML NPLs with an average diameter of 10 nm and square shape of 2 ML and 3 ML NPLs with an average lateral size of 12 and 20 nm, respectively.

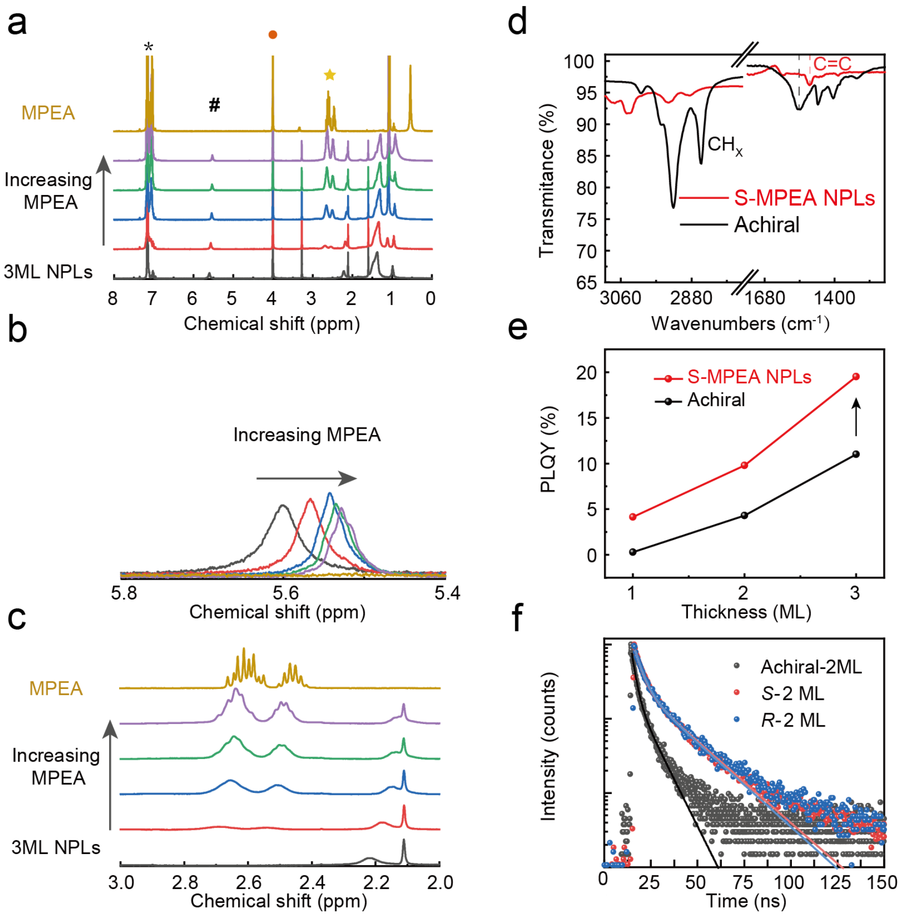

Figure 3. (a) ^1H NMR spectra and (b-c) enlarged ranges of the NMR spectra of 3 ML $CsPbBr_3$ NPLs with increasing amount (see **Experiment Section**) of S-MPEA and of the NMR spectra of pure S-MPEA(dark yellow) in C_6D_6 (denoted by *); vinyl group (δ = 5.5–5.6 ppm) is denoted with #; alkyl groups of MPEA (δ = 2.2–2.8 ppm) is denoted by yellow star symbol; resonance of internal ferrocene standard is denoted by orange spot; (d) FTIR spectra of 3 ML $CsPbBr_3$ NPLs before (red) and after (black) ligand exchange; (e) PLQY of MHP NPLs with different thicknesses before and after ligand exchange; (f) TRPL decay curves of 2 ML $CsPbBr_3$ NPLs before and after ligand exchange with *S*-MPEA and *R*-MPEA.

Chiral amine *S*- or *R*-MPEA are then introduced into colloidal achiral perovskite NPLs by a ligand exchange reaction. Superstoichiometric chiral amine is added to colloidal NPLs and shaken vigorously to allow sufficient ligand exchange. No further purification is conducted because more than one purification cycle will cause NPLs to aggregate due to the loss of surface ligands.

In-situ solution ^{1}H NMR experiments were first used to probe the ligand exchange reactions, where chiral MPEA ligands were gradually added into the achiral NPL solutions (**Figures 3a-c**, **S3**). The native ligands of perovskite nanocrystals are generally described as dynamic pairs of cations ($RCH_2NH_3^+$) and anions ($RCOO^-$)[18, 19].With increasing amount of MPEA ligands (see **Experiment Section**) added to the 2–3 ML NPLs, the broad peak associated with the vinyl group of oleylammonium at 5.6 ppm becomes sharper and shifts upfield into the free oleylammonium resonance (**Figure 3b**, **Figure S3b**), suggesting the removal of oleylammonium ligands. For 1 ML NPLs capped without oleylamine, the peak around 5.5 ppm associated with the vinyl group of native oleic acid does not change, while the alkyl resonance ($\delta = 2.0–2.15$ ppm) of native bound ammonium disappears with the addition of MPEA ligands (**Figure S3e**). In addition, the broad peaks associated with the alkyl groups of MPEA ($\delta = 2.2–2.8$ ppm) increase gradually (**Figure 3c, Figure S3c, f**) in 1–3 ML NPLs. Taken together, our NMR experiments suggest that chiral MPEA can replace native ammonium ligands while leaving oleic acid unexchanged. We propose that the ligand exchange reaction proceeds as follows:

$$\mathrm{NPL}\ (RCOO^-)(RCH_2NH_3^+) + \mathrm{MPEA} \rightarrow \mathrm{NPL}\ (RCOO^-)(\mathrm{MPEAH}^+) + RCH_2NH_2$$

where $RCOO^-$ stands for oleic acid and $RCH_2NH_3^+$ is octyl-, butyl-, or oleyl ammonium. During the ligand exchange reaction, chiral MPEA can quantitatively or near-quantitatively replace native ammonium ligands, creating chiral perovskite NPLs.

Fourier-transform infrared (FT-IR) spectroscopy is also used to confirm the proposed surface exchange reaction of perovskite NPLs. Taking 3 ML $CsPbBr_3$ NPLs as an example, the achiral NPLs show several peaks due to the presence of native ligands, that is, oleate acid (OA) and OAm. The peaks at ν=2850–3000 cm^{-1} and ν=1461 cm^{-1} typically indicate asymmetric and symmetric stretching of C–H from both OA and OAm[20]. The peak at ν=1540 cm^{-1} corresponds to the COO^- symmetric stretching mode of OA[19, 21] For ligand-exchanged perovskite NPLs, the FT-IR spectra show a decreased intensity of C–H vibrations in the 2850–3000 cm^{-1} region and new peaks appear at and 1500 cms^{-1} which are associated with C=C stretching vibrations of aromatic hydrocarbons[7].

Optical properties of the ligand-exchanged perovskite NPLs are then probed by a wide array of steady-state and time-resolve spectroscopic techniques. UV-vis absorption spectra (**Figure S5**) exhibit nearly no shifts of the first exciton peak compared to those with native ligands, indicating the same nanocrystal morphology. To further probe the impact of ligand exchange on the PL properties, we measure their PLQY. As illustrated in **Figure 3b** and **Table 1**, the PLQY is generally improved with thicker perovskite NPLs. Additionally, we observe a significant improvement of PLQY after the post-synthetic ligand treatment. For 1 ML NPLs, a more than tenfold PLQY increase (from 0.28% to above 3.33%) is observed. For 2 and 3 ML NPLs, the PLQY is improved by nearly a factor of two, with the highest PLQY of 18–19 % obtained in ligand-exchanged 3 ML NPLs. The observed PLQY enhancement in thicker perovskite NPLs is consistent with previous reports[16]. To understand the PLQY enhancement, we collect time-resolved photoluminescence (TRPL). The PL decay is fitted with a bi-exponential decay function (Eq. S1 in Supporting Information). As illustrated in **Figure 3c**, **Figure S4**, and **Table 1**, the average PL lifetime (τ_A, Eq S2) of perovskite NPLs with various thicknesses all increase upon ligand exchange. Combined with their measured PLQY, we calculated their radiative (k_r) and nonradiative recombination rates (k_{nr}) (results shown in **Table 1**). Notably, k_{nr} decreases upon ligand exchanged with chiral amines, i.e., from 0.38 to 0.24 ns^{-1} (1 ML NPLs), from 0.16 to 0.06 ns^{-1} (2 ML NPLs) and from 0.30 to 0.20 ns^{-1} (3 ML NPLs), respectively. We attribute this decline of nonradiative process to an enhanced surface passivation of defect states. The synthesized NPLs suffer from ligand-detaching after the purification process, resulting in surface defects.

Table 1 Fitting results of PL decay curves, PLQY, calculated radiative and non-radiative recombination rates of MHP NPLs with different thicknesses before and after ligands exchange.

Entry	τ_1 (ns)	τ_2 (ns)	τ_A (ns)	k_r (ns^{-1})	k_{nr} (ns^{-1})	PLQY
1 ML Achiral	1.04	3.85	2.59	0.0011	0.3844	0.28%
R-1 ML	1.68	15.74	4.10	0.0081	0.2360	3.33%
S-1 ML	1.61	15.53	3.93	0.0105	0.2438	4.14%
2 ML Achiral	2.13	8.60	5.88	0.0073	0.1628	4.3%
R-2 ML	4.07	19.17	14.26	0.0069	0.0632	9.9%
S-2 ML	3.88	19.81	14.88	0.0066	0.0606	9.8%
3ML Achiral	1.15	3.52	2.94	0.0374	0.3025	11.0%
R-3 ML	2.58	6.42	4.21	0.0427	0.1946	18.0%
S-3 ML	2.37	6.14	3.97	0.0491	0.2026	19.5%

The subsequent addition of chiral MPEA ligands absorbed on the surface of perovskites NPLs can effectively passivate those trap states[22]. Therefore, the likelihood of nonradiative recombination processes is reduced by chiral ligands. In addition, the enhanced PLQY and PL lifetime further support that chiral amine molecules are effectively attached to NPLs surfaces.

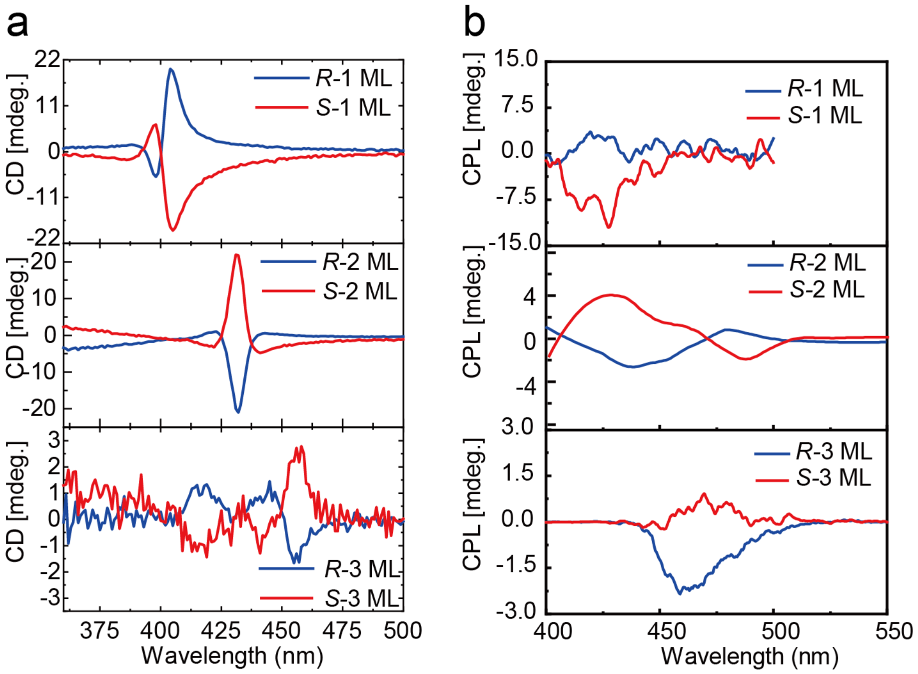

Figure 4. (a) CD spectra and (b) CPL spectra of as synthesized MHP NPLs of 1, 2 and 3 ML thickness.

With the attached chiral surface ligands on perovskite NPLs (1, 2, 3 MLs), we then study their optical activity using CD and CPL spectroscopy. All samples are tested in the toluene. The CD spectra of chiral $CsPbBr_3$ NPLs (**Figure 4a**) of different handedness are mirror images of one another, with strong CD signals at their first exciton peak positions (**Figure 2a**), confirming the successful chirality transfer from organic to the inorganic phase. The CD response shifts to lower energy with the increase of layer thickness, consistent with the change of their optical bandgaps due to the quantum confinement effect. 1 ML NPLs display the largest CD response, which decreases with the increase of NPL thickness. Strong derivative features at their exciton peaks are observed in 1 and 3 ML NPLs, while 2 ML NPLs exhibit less obvious Cotton effect. Interestingly, the CD signal with the same chirality of ligands switches its sign from 1 to 2 ML NPLs (**Figure 4a**). We tentatively attribute this to a different prototype of distortion in the lattice of 1 ML NPLs, which results in a change in the angle between the magnetic and transition state dipole. A more quantitative explanation would require more work, which is out of the scope of current study. In 3 ML NPLs, clear bisignate CD signals are observed in both the first exciton (~450 nm) and second exciton (~420 nm) transitions. Noticeably, our chiral MHP NPLs present a considerable room temperature CPL signal (**Figure 4b**), which has not been observed in previously reported 2D all inorganic chiral perovskite NPLs[8]. The CPL signal also shifts to lower energies with a decreased intensity from 1 to 3 ML NPLs. CPL signals of 1 and 3 ML NPLs exhibit clear bisignate peaks with the opposite chirality; however, CPL signals in

2 ML NPLs appear to consist of signals from both 2 and 3 ML NPLs. This is due to the sample instability in 2 ML NPLs despite of many attempts to stabilize it. However, we can still quantitatively extract the asymmetry factors based on their PL wavelength of 1–3 ML NPLs.

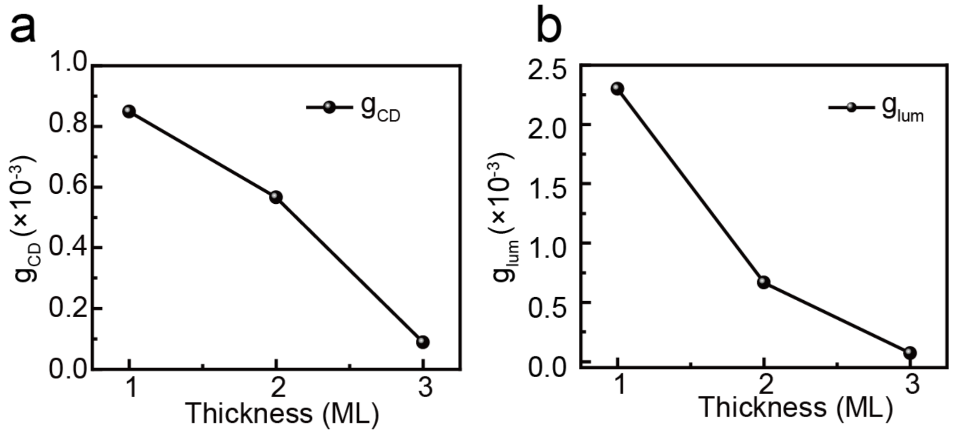

Figure 5. (a)Thickness-dependent g_{CD}, (b) g_{lum} for *S*-MPEA modified MHP NPLs.

To further quantify the chiroptical properties, the *g*-factor of CD (g_{CD}) and CPL (g_{lum}) signals are calculated. g_{CD} is calculated according to the following equation:

$$g_{CD} = \frac{\Delta\varepsilon}{\varepsilon} = (A_L - A_R)/A = \theta[mdeg]/(32980A) \qquad \text{Eq. (1)}$$

where the A_L and A_R represent left and right circularly polarized light absorbance, A is linear light absorbance, and $\theta[mdeg]$ is corresponding CD signal peak intensity in mDegree. The calculated g_{CD} at the first exciton peaks of perovskite NPLs are all in the order of 10^{-4} for 1–3 MLs. g_{CD} as the function of layer thickness of *S*-chiral NPLs is plotted in **Figure 5a** and **Figure S6a** (*R*-chiral NPLs**)**. The values of g_{CD} decreases gradually with the increase of layer thickness.

The dissymmetry factor of luminescence(g_{lum}) is also calculated as follows:

$$g_{lum} = 2 \times \frac{I_L - I_R}{I_L + I_R} \qquad \text{Eq. (2)}$$

where the I_L and I_R are the intensity of left- and right-handed CPL at a given wavelength. The obtained g_{lum} as a function of layer thickness is plotted (**Figure 5b** and **Figure S6b**). In *S*-MPEA capped NPLs, the maximum g_{lum} value is determined as 2.30×10^{-3}, 6.67×10^{-4}, and 7.0×10^{-5} for 1, 2, 3 ML NPLs, respectively. In *R*-MPEA modified NPLs, the g_{lum} value is calculated as 6.70×10^{-4}, 4.2×10^{-4}, and 1.80×10^{-5} for 1, 2, 3 ML NPLs, respectively. Similar to the trend of g_{CD}, g_{lum} decreases as NPLs thickness increases. However, the decreased dissymmetry factors are accompanied with an increase in PLQY at thicker perovskite NPLs due to the larger fraction of surface defect density present in thinner NPLs. Considering these two factors, 2 ML $CsPbBr_3$ capped with chiral ligands is believed to possess relatively better CPL performance.

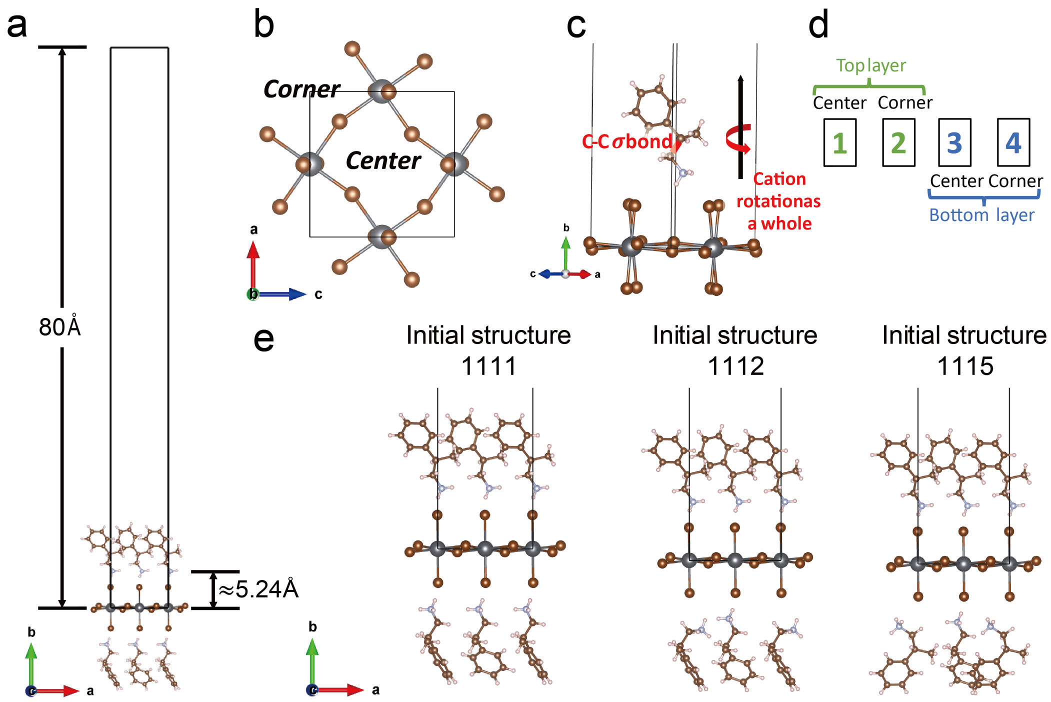

Figure 6. (a) An example of the monolayer slab models with *R*-MPEA ligands attached on opposite surfaces. (b) A top-view of the c(2×2) unit cell showing the two cation adsorption sites (corner site and center site). After considering the top and bottom surfaces of each slab, four independent organic ligands were considered in our geometry enumeration. (c) A conceptual figure showing the two discrete conformational differences of an organic ligand attached on the inorganic slab: 1) the orientation of the aminomethyl group; 2) the cation rotation as a whole with respect to the inorganic substrate. (d) The meaning of a 4-digit identification code for ligand adsorption structures as used in our study. The first two values represent the center- and corner-site ligands of the top organic layer and the last two values represent the center- and corner-site ligands of the bottom organic layer. (e) Three examples of the 4-digit code and their corresponding initial geometries for DFT relaxation.

The optical activity suggests that the spin-degeneracy of optical transitions is lifted in chiral perovskite NPLs; however, it is unclear what mechanism leads to the spin splitting from a structural perspective. We envision that the chiral perovskite NPLs provide a unique platform to understand the chirality transfer mechanism. On one hand, thinner perovskite NPLs possess larger bandgaps, which might result in a stronger electronic interaction between the organic and inorganic phases as their frontier orbital energies approach each other. On the other hand, thinner NPLs also exhibit larger surface-to-volume ratio, which will lead to relatively more chiral ligands on the surfaces of NPLs compared to the overall amount of metal halide. Although both effects can account for the larger optical activity in thinner perovskite NPLs, it is unclear which mechanism plays a more dominant role.

To determine the degree of structural chirality in the perovskite NPLs, we perform first-principles calculations to analyze the energetically preferred structure, chirality and spin properties of the perovskite NPLs. One general challenge of simulating nano-scale systems is that their detailed atomic structures are usually unknown since methods such as single-crystal X-ray diffraction are generally not applicable to aggregates of nanoscale objects. In reference 2, some of us studied the depth dependence of chiral-induced distortions in perovskite nanocrystals, approximating the expected surface structure of a relatively thick structure with the known arrangement in a layered perovskite (1-(1-naphthyl) ethylammonium lead bromide)[23]. In the present work, we take a much more rigorous approach to identify the probable ligand adsorption geometries at thin (essentially, all-surface) nanoplatelets by computational means. Specifically, we know little about the conformation of the organic cations and how they interact with the inorganic substrate. Instead of purely relying on the crystal structures of 2D hybrid perovskites and assuming organic cations to behave similarly, we aim to construct nanoplatelet models from scratch, based on a systematic enumeration of possible adsorption geometries. We subsequently perform direct structure optimizations using van der Waals corrected[24] semilocal DFT[25], a level of theory well suited for faithful structure prediction of complex organic-inorganic hybrid perovskite in past work by our group.[23, 26]

We begin from the "c(2×2)" unit cell (see **Figure 6b** for a depiction) of a perovskite layer of $CsPbBr_3$ to construct the inorganic component of the NPLs[27]. The original 3D orthorhombic bulk structure is cut (along the (101) plane) into 2D slabs containing one or two octahedrons in thickness, to model the monolayer and bilayer NPLs. As shown in **Figure 6a**, the inorganic slab extends along the (a,c) plane, and the lattice vector b is set to 80 Å to avoid possible interactions between adjacent slabs. In each 2D c(2×2) unit cell, two cation absorption sites (corner site and center site) exist on either side of the slab, leading to a total of four independent organic cation ligands in each unit cell (considering the top and bottom surfaces, shown in **Figure 6a** and **6b**). We then conduct a systematic conformation enumeration for those organic ligands. In an *R*-MPEA cation, the rotation of sigma bonds determines the overall molecular conformation **(Figure 6c)**. Still, most functional groups can undergo low-barrier rotations (for example, the methyl group, the amino group, and the phenyl group). In our study, the only rigid conformational feature in *R*-MPEA is the orientation of the aminomethyl group, modulated by its interaction with the inorganic substrate. We consider the rotation of this group by 0°, 90°, 180°, and 270° to create four possible intra-molecule conformations. Together with the two possible orientations (rotated by 0° and 90°) of the whole cation with respect to the perovskite substrate, each *R*-MPEA cation has eight possible conformations on its absorption site **(Figure 6c)**. To concisely represent the conformations of all four *R*-MPEA cations, we employ a 4-digit code (representing the four independent cations in a unit cell) and each digit can assume a value from 1 to 8 (representing the eight different conformations of a *R*-MPEA cation) as shown in **Figure 6d**. Examples of the 4-digit numbers and their corresponding initial geometries, prior to structure optimization, are shown in **Figure 6e**.

Following the geometry enumeration strategy above, two sets of input structures were constructed for monolayer and bilayer slab models (with *R*-MPEA cations on both surfaces), each containing $8^4 = 4{,}096$ initial geometries. Starting from these geometries, we conducted high-throughput DFT relaxations utilizing the world-class GPU-accelerated supercomputer Perlmutter (at the National Energy Research Scientific Computing Center) and the GPU-accelerated FHI-aims code[28, 29] with "light" settings. Relative total energies of all relaxed structures with respect to the most stable one in each set are shown in **Figure S7**. Different initial conformations of the organic cations can cause significant energy differences (up to ~2.5 eV in monolayer models and up to ~1.6 eV in bilayer models) in the relaxed structures, and we attribute the less-dispersed total energy values in bilayer models to the more rigid inorganic substrate. When considering the thermal fluctuation at room temperature ($k_bT_r \approx 26$ meV), a limited portion of the relaxed structures have “indistinguishable” total energies compared to the most stable one. Thus, these structures compose the output of our geometry prediction.

Many publications emphasize the central role of inorganic distortion in the perovskite band structure and spin-splitting[2, 23, 30]. Therefore, we analyzed the predicted stable geometries and found three distortion prototypes (i.e., 18 relaxed systems fall into three similar structures) for the monolayer model and two distortion prototypes (i.e., 11 relaxed systems fall into two similar structures) for the bilayer model (shown in Supporting Information **Figure S8** and **S9**). Using one representative structure for each distortion prototype, we further relaxed them using stricter settings (FHI-aims NAO basis sets with “intermediate” numerical defaults) and conducted electronic structure calculations using the DFT-PBE density functional including spin-orbit coupling[31]. Conceptual figures of the real-space 2D unit cell, the reciprocal 2D unit cell, and high-

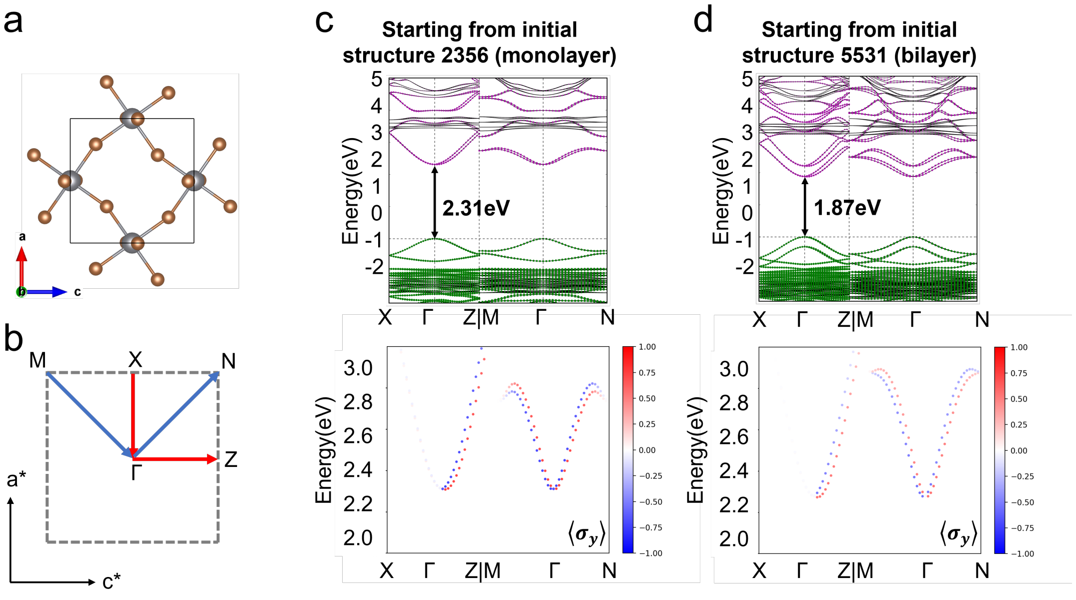

Figure 7. (a) A top-view of the real-space c(2×2) unit cell. (b) High-symmetry points and k-space paths included in the band structures of MHP slab models. (c,d) DFT-PBE+SOC based band structure and the most significant spin texture components of their lowest conduction bands for two representative monolayer and bilayer MHP slab models.

symmetry *k* points sampled in the band structure calculations are shown in **Figure 7a** and **7b**. **Figure S10** in the Supporting Information consist of all PBE+SOC band structures and the most significant spin textures component ($\langle\sigma_y\rangle$) of their lowest conduction bands. We here use the PBE density functional for band structure calculations since our objective is to analyze spin-orbit coupling, which is a large qualitative effect based on the character of the eigenstates and already well represented at this computationally affordable level of theory[31]. Two representative examples are shown in **Figure 7c** and **7d**. In general, inorganic elements are the dominant contributors to the band edges both in the monolayer and bilayer slab models, and negligible contributions from organic components in the band edges are found in 1–2 ML NPLs. By reducing the quantum confinement in the inorganic moiety, the bilayer slab models have a significantly smaller fundamental bandgap (~1.9 eV) than the monolayer slab models (~2.3 eV). All these features are consistent with the experimental UV-vis absorption observations. Additionally, spin texture calculations[23] further confirm the existence of spin-splitting in the conduction bands (**Figure 7c-d**). This information indicates an overall chirality mainly due to the symmetry breaking in the inorganic substrate and supports the active CD and CPL signals in experiments. Different monolayer and bilayer models show spin splittings between ~4 and 20 meV (Table S6) in their band segments, but not with an unambiguous trend (i.e., spin splitting values above 15 meV can be achieved for both low-energy monolayer and bilayer models). In view of the trend of chiroptical activity (rather than just spin splitting), further factors can play a role. For instance, in Table S6, the absolute values of the $\langle\sigma_y\rangle$ at the CBM are shown to be somewhat larger for the monolayer models than for the bilayer models that we examined. Furthermore, in the presence of an actual electronic excitation, monolayers may be structurally more flexible (and thus more prone to further structural distortions) than bilayers, although we cannot determine this from ground-state DFT. Regarding the three-layer case (which we did not predict in DFT for reasons of computational cost), it is expected that the central layer, which is not exposed to the surface, will be less prone to structural distortion than the monolayer and bilayer case, i.e., the degree of symmetry breaking is larger in thinner MHP NPLs. Therefore, the trends of dissymmetry factors with changed thickness collected in experiments is rational.

Conclusion

In summary, we successfully realize tunable CPL in the deep blue to blue spectrum from chiral perovskites NPLs for the first time in the strong quantum confined regime. The chiral *R*- and *S*-MPEA ligands are functionalized onto perovskite NPL surface via a facile ligand exchange strategy, which endows MHP chirality and passivate surface defects simultaneously. Spectroscopic investigations indicate that thinner NPLs possess larger surface defects and lower PLQY, but their large surface-to-volume ratio and more flexible lattices leads to stronger chirality transfer from surface chiral ligands. Our computational results suggest that the chirality mainly originates from inorganic lattice distortions induced by the chiral surface and has little contribution from direct orbital hybridization between the organic and inorganic components. Our work provides an important strategy for optical activity manipulation and offers a better understanding towards chirality transfer mechanism from organic molecules to inorganic perovskites in the nanoscale.

Methods

Materials. Lead bromide ($PbBr_2$, Macklin, 99.99%), oleic acid (OA, Aladdin, 90%), oleylamine (OAm, Aladdin, 70%), toluene (C_7H_8, Sinopharm, AR), cesium bromide (CsBr, Aladdin, 99%), acetonitrile (C_2H_3N, Aladdin, AR), N, N-dimethylformamide (DMF, Sinopharm, AR). n-Octylammonium Bromide (Lumtec, >99.5%), n-Butylammonium bromide (Lumtec, >99.5%), (S)-β-Methylphenethylamine (S-MPEA, Sigma, 99%), (R)-(+)-β-Methylphenethylamine (R-MPEA, Aladdin, >98.0%(GC)), All chemicals were used as received without any purification.

Preparation of CsBr stock solution.

64 mg of CsBr (0.3 mmol) is dissolved into 15 mL of DMF at room temperature under an ambient atmosphere. The as-prepared DMF stock solution containing 0.02 M CsBr is stored at 4 °C for further use.

Preparation of LBr (L= octylammonium or butylammonium) stock solution.

1 mmol of LBr is dissolved in to 10 mL of DMF at room temperature under an ambient atmosphere. The as-prepared DMF stock solution containing 0.1 M LBr is stored at 4 °C for further use.

Synthesis of 1 ML perovskite NPLs.

0.5 mL octylammonium bromide, 0.5 mL butylammonium bromide and 10 μL OA precursor solution are mixed at room temperature. 0.05 mmol $PbBr_2$ is dissolved into as prepared ammonium bromide solution. 20 μL mixture is quickly injected to 5 mL toluene undergoing vigorous stirring for 2 min. The crude product solution is first centrifuged at 3500 rpm for 3 min to remove unreacted materials and aggregated precipitates. Finally, the single layer $[PbBr_4]^{2-}$ NPLs are collected by centrifuging at 12000 rpm for 3 min and redispersed in toluene. Additional 1 μL OA is added for better dispersion of NPLs.

Synthesis of 2-ML and 3-ML $CsPbBr_3$ NPLs.

In typical experiments, 110 mg of $PbBr_2$ (0.3 mmol) is added into 1.50 mL of DMF. After complete dissolving of $PbBr_2$, OA (0.15 mL) and OAm (1.5 mL) are added, followed by the addition of CsBr precursor solution (0.20 mL for 2-ML NPLs, 0.40 mL for 3-ML NPLs). Finally, the mixture (0.35 mL for 2-ML NPLs, 0.7 mL for 3-ML NPLs) is quickly added into a reaction flask containing 10 mL of toluene under vigorous stirring to initiate the formation of $CsPbBr_3$ nanocrystals.

After the reaction for 20~60 s, the reaction is terminated by the addition of acetonitrile (10 mL). The as prepared nanoplatelets are collected by centrifugation at 12000 rpm for 6 minutes followed by redispersion in 5 mL of toluene.

Induction of Chirality in perovskite NPLs.

Superstoichiometric (4 μL, ~28 μmol) *S*- or *R*-MPEA is added in to 2 mL of purified NPLs and shacked under the vortex mixer. After ligand exchange, the mixture is centrifuged at 3000 rpm for 5 min to remove aggregates due to the loss of ligands during the process.

Characterization method

Powder X-ray diffraction (XRD) patterns are recorded on an Empyrean PANanalytical diffractometer with an ADDS wide-angle X-ray powder diffractometer (Cu Kα radiation, λ = 1.54184 Å). **Nuclear Magnetic Resonance (NMR)** are collected on a Bruker AVII 400 MHz

NMR Spectrometer. This spectrometer is equipped with a PA BBO 400SB BBFO-H-D05 Z-gradient BB observe probe head, BB=^{19}F-^{31}P-^{15}N; with Z-gradient with active shielding for 5 mm and ATM accessory. **In-situ NMR Experiment**. Perovskite NPLs were collected by centrifugation and redispersed in deuterated. 0.6 mL of NPL solution was loaded in an NMR tube. 3.3 μmol ferrocene was added as an internal standard. 0.5 μL *S*-MPEA was then added into the NMR tube each time. Ligand exchange reaction was promoted by shaking the NMR tube for 5 min. ^{1}H NMR spectrum was then collected after each addition of *S*-MPEA. **UV-vis absorption spectroscopic** measurements are performed using a UH5700 spectrophotometer. The scans are performed for a wavelength range of 380 nm – 550 nm, with 1 nm step size and repetition of one cycle. The nanoplatelets sample is dispersed in toluene and loaded in a 10 mm × 10 mm quartz cuvette in colloidal form. **Photoluminescence (PL) spectra** are recorded using a fluorescence spectrometer (FS5, Edinburgh) equipped with a xenon lamp, the excitation wavelength is 360 nm. **The absolute photoluminescence quantum yield (PLQY)** of the samples in toluene are measured using an FS5 spectrofluorometer with a SC-30 integration sphere, Edinburg instruments. **Circular dichroism (CD) spectra** are measured by Chirascan™ Circular Dichroism Spectrometer (by Applied Photophysics Ltd) for a wavelength range of 360 nm – 500 nm with 1 nm resolution at room temperature. The spectra are obtained by one scan. The samples are prepared in the same method of UV-vis absorption spectroscopic measurement sample. The analysis of the layers is conducted with **atomic force microscopy (AFM)** measurement by using a Nanoscope IIIa/Dimension 3100 (Digital Instrument) in the tapping mode. The **Circularly Polarized Luminescence (CPL)** spectra of samples in toluene are recorded by ASCO CPL-300 spectrometer at room temperature. **Time-resolved PL spectra** was obtained using a pulsed laser excitation from a Ti:sapphire oscillator (Coherent Mira900, 100 fs) through a pulse picker and tuned to 730 nm and frequency doubled to give 365 nm. The PL is collected and analysed by a spectrometer (Acton SpectraPro 257) to disperse the PL from the centre wavelength onto a photon counter, and time correlated single photon counting is carried out using a Becker and Hickl system (SPC150). **Fourier Transform Infrared Spectroscopy** (FT-IR) is performed using Bruker Tensor 27 FT-IR Spectrometer.

First-principles calculations

We employ the GPU-accelerated [29]all-electron electronic structure code FHI-aims[28] to perform the DFT simulations. A total of 8,192 different input geometries and (3 × 1 × 3) k-grids for each of them are processed using a massively parallel, high-throughput DFT approach. Numeric atom-centered orbital (NAO) basis sets in FHI-aims with “light” numerical default settings, the ELSI infrastructure[32] and GPU acceleration for DFT[29] are employed in the step of high-throughput geometry relaxations. In subsequent steps and for the lowest-energy target structures, we employ to NAO basis sets with “intermediate” numerical default settings. All geometry relaxations were based on the PBE functional[25] with a modified Tkatchenko-Scheffler dispersion energy correction[2, 24], and all band structure and spin texture calculations are based on the PBE functional plus second-variational non-self-consistent spin-orbit coupling[31].

Acknowledgments

We gratefully acknowledge the start-up funding support from the Hong Kong University of Science and Technology (HKUST) School of Science (SSCI) and the Department of Chemistry (R9270). This work was also supported by the Research Grants Council of Hong Kong via the Early Career Scheme (ECS, 26300721) and the National Natural Science Foundation of China (Grant No. 22205186). R. S. and V.B. were supported by the National Science Foundation under Awards No. ACI-1450280 and DMR-1729297. This research used resources of the National Energy Research Scientific Computing Center (NERSC), a U.S. Department of

Energy (DOE) Office of Science User Facility operated under Contract no. DEAC02-05CH11231.

Data availability

Atomic structure information of the lowest-energy monolayer and bilayer MHP slabs discussed in this work is provided in the SI. The full set of computational high-throughput calculations for 8,192 relaxes structure candidates will be made publicly available at the NOMAD repository with a permanent DOI at the time of publication.

Conflicts of interest

V.B. is a board member of MS1P e.V., the non-profit organization that licenses the FHI-aims code used in this work. He does not derive any financial gains from this position. All other authors have no conflicts to declare.

References

(1) Lu, H.; Vardeny, Z. V.; Beard, M. C. Control of light, spin and charge with chiral metal halide semiconductors. *Nature Reviews Chemistry* **2022**, *6* (7), 470-485. DOI: 10.1038/s41570-022-00399-1. Kim, Y. H.; Zhai, Y.; Gaulding, E. A.; Habisreutinger, S. N.; Moot, T.; Rosales, B. A.; Lu, H.; Hazarika, A.; Brunecky, R.; Wheeler, L. M.; et al. Strategies to Achieve High Circularly Polarized Luminescence from Colloidal Organic-Inorganic Hybrid Perovskite Nanocrystals. *ACS Nano* **2020**, *14* (7), 8816-8825. DOI: 10.1021/acsnano.0c03418. Kim, Y.-H.; Zhai, Y.; Lu, H.; Pan, X.; Xiao, C.; Gaulding, E. A.; Harvey, S. P.; Berry, J. J.; Vardeny, Z. V.; Luther, J. M.; et al. Chiral-induced spin selectivity enables a room-temperature spin light-emitting diode. *science* **2021**, *371*. Kotov, N. A.; Liz-Marzán, L. M.; Weiss, P. S. Chiral Nanostructures: New Twists. *ACS Nano* **2021**, *15* (8), 12457-12460. DOI: 10.1021/acsnano.1c06959. Shi, Y.; Duan, P.; Huo, S.; Li, Y.; Liu, M. Endowing Perovskite Nanocrystals with Circularly Polarized Luminescence. *Adv Mater* **2018**, *30* (12), e1705011. DOI: 10.1002/adma.201705011.

(2) Kim, Y. H.; Song, R.; Hao, J.; Zhai, Y.; Yan, L.; Moot, T.; Palmstrom, A. F.; Brunecky, R.; You, W.; Berry, J. J.; et al. The Structural Origin of Chiroptical Properties in Perovskite Nanocrystals with Chiral Organic Ligands. *Advanced Functional Materials* **2022**, *32* (25). DOI: 10.1002/adfm.202200454.

(3) Chen, W.; Zhang, S.; Zhou, M.; Zhao, T.; Qin, X.; Liu, X.; Liu, M.; Duan, P. Two-Photon Absorption-Based Upconverted Circularly Polarized Luminescence Generated in Chiral Perovskite Nanocrystals. *J Phys Chem Lett* **2019**, *10* (12), 3290-3295. DOI: 10.1021/acs.jpclett.9b01224.

(4) Assaf Ben Moshe; Daniel Szwarcman; Markovich, G. Size Dependence of Chiroptical Activity in Colloidal Quantum Dots. *ACS Nano* **2011**, *5*, 10.

(5) Moloney, M. P.; Gun'ko, Y. K.; Kelly, J. M. Chiral highly luminescent CdS quantum dots. *Chem Commun (Camb)* **2007**, (38), 3900-3902. DOI: 10.1039/b704636g.

(6) Elliot, S. D. Chiral Shells and Achiral Cores in CdS Quantum Dots. *J Am Chem Soc* **2008**, *8*, 2452-2457.

(7) Jiang, S.; Song, Y.; Kang, H.; Li, B.; Yang, K.; Xing, G.; Yu, Y.; Li, S.; Zhao, P.; Zhang, T. Ligand Exchange Strategy to Achieve Chiral Perovskite Nanocrystals with a High Photoluminescence Quantum Yield and Regulation of the Chiroptical Property. *ACS Appl Mater Interfaces* **2021**, *14*, 3385–3394. DOI: 10.1021/acsami.1c18978.

(8) Ren, H.; Wu, Y.; Wang, C.; Yan, Y. 2D Perovskite Nanosheets with Intrinsic Chirality. *J Phys Chem Lett* **2021**, *12* (10), 2676-2681. DOI: 10.1021/acs.jpclett.1c00315.

(9) Hubley, A.; Bensalah-Ledoux, A.; Baguenard, B.; Guy, S.; Abécassis, B.; Mahler, B. Chiral Perovskite Nanoplatelets Exhibiting Circularly Polarized Luminescence through Ligand Optimization. *Advanced Optical Materials* **2022**, 2200394. DOI: 10.1002/adom.202200394.

(10) Georgieva, Z. N.; Bloom, B. P.; Ghosh, S.; Waldeck, D. H. Imprinting Chirality onto the Electronic States of Colloidal Perovskite Nanoplatelets. *Adv Mater* **2018**, *30* (23), e1800097. DOI: 10.1002/adma.201800097.

(11) Zhou, Y.; Zhu, Z.; Huang, W.; Liu, W.; Wu, S.; Liu, X.; Gao, Y.; Zhang, W.; Tang, Z. Optical coupling between chiral biomolecules and semiconductor nanoparticles: size-dependent circular dichroism absorption. *Angew Chem Int Ed Engl* **2011**, *50* (48), 11456-11459. DOI: 10.1002/anie.201103762.

(12) Gao, X.; Zhang, X.; Zhao, L.; Huang, P.; Han, B.; Lv, J.; Qiu, X.; Wei, S. H.; Tang, Z.

Distinct Excitonic Circular Dichroism between Wurtzite and Zincblende CdSe Nanoplatelets. *Nano Lett* **2018**, *18* (11), 6665-6671. DOI: 10.1021/acs.nanolett.8b01001.

(13) Gao, X.; Han, B.; Yang, X.; Tang, Z. Perspective of Chiral Colloidal Semiconductor Nanocrystals: Opportunity and Challenge. *J Am Chem Soc* **2019**, *141* (35), 13700-13707. DOI: 10.1021/jacs.9b05973. Forde, A.; Ghosh, D.; Kilin, D.; Evans, A. C.; Tretiak, S.; Neukirch, A. J. Induced Chirality in Halide Perovskite Clusters through Surface Chemistry. *The Journal of Physical Chemistry Letters* **2022**, *13* (2), 686-693. DOI: 10.1021/acs.jpclett.1c04060.

(14) Cao, Q.; Ilyas, A.; Zhang, S.; Ju, Z.; Sun, F.; Liu, T.; Yang, Y. M.; Lu, Y.; Liu, X.; Deng, R. Lanthanide-doping enables kinetically controlled growth of deep-blue two-monolayer halide perovskite nanoplatelets. *Nanoscale* **2021**, *13* (26), 11552-11560. DOI: 10.1039/d1nr02508b.

(15) Polavarapu, L.; Nickel, B.; Feldmann, J.; Urban, A. S. Advances in Quantum-Confined Perovskite Nanocrystals for Optoelectronics. *Advanced Energy Materials* **2017**, *7* (16), 1700267. DOI: 10.1002/aenm.201700267.

(16) Bohn, B. J.; Tong, Y.; Gramlich, M.; Lai, M. L.; Doblinger, M.; Wang, K.; Hoye, R. L. Z.; Muller-Buschbaum, P.; Stranks, S. D.; Urban, A. S.; et al. Boosting Tunable Blue Luminescence of Halide Perovskite Nanoplatelets through Postsynthetic Surface Trap Repair. *Nano Lett* **2018**, *18* (8), 5231-5238. DOI: 10.1021/acs.nanolett.8b02190.

(17) Brennan, M. C.; Herr, J. E.; Nguyen-Beck, T. S.; Zinna, J.; Draguta, S.; Rouvimov, S.; Parkhill, J.; Kuno, M. Origin of the Size-Dependent Stokes Shift in CsPbBr(3) Perovskite Nanocrystals. *J Am Chem Soc* **2017**, *139* (35), 12201-12208. DOI: 10.1021/jacs.7b05683.

(18) De Roo, J.; Ibanez, M.; Geiregat, P.; Nedelcu, G.; Walravens, W.; Maes, J.; Martins, J. C.; Van Driessche, I.; Kovalenko, M. V.; Hens, Z. Highly Dynamic Ligand Binding and Light Absorption Coefficient of Cesium Lead Bromide Perovskite Nanocrystals. *ACS Nano* **2016**, *10* (2), 2071-2081. DOI: 10.1021/acsnano.5b06295.

(19) Wheeler, L. M.; Sanehira, E. M.; Marshall, A. R.; Schulz, P.; Suri, M.; Anderson, N. C.; Christians, J. A.; Nordlund, D.; Sokaras, D.; Kroll, T.; et al. Targeted Ligand-Exchange Chemistry on Cesium Lead Halide Perovskite Quantum Dots for High-Efficiency Photovoltaics. *J Am Chem Soc* **2018**, *140* (33), 10504-10513. DOI: 10.1021/jacs.8b04984.

(20) Safo, I. A.; Dosche, C.; Ozaslan, M. Effects of Capping Agents on the Oxygen Reduction Reaction Activity and Shape Stability of Pt Nanocubes. *Chemphyschem* **2019**, *20* (22), 3010-3023. DOI: 10.1002/cphc.201900653.

(21) Ibarra, J.; Melendres, J.; Almada, M.; Burboa, M. G.; Taboada, P.; Juárez, J.; Valdez, M. A. Synthesis and characterization of magnetite/PLGA/chitosan nanoparticles. *Materials Research Express* **2015**, *2* (9), 095010. DOI: 10.1088/2053-1591/2/9/095010.

(22) Li, G.; Huang, J.; Zhu, H.; Li, Y.; Tang, J.-X.; Jiang, Y. Surface Ligand Engineering for Near-Unity Quantum Yield Inorganic Halide Perovskite QDs and High-Performance QLEDs. *Chemistry of Materials* **2018**, *30* (17), 6099-6107. DOI: 10.1021/acs.chemmater.8b02544.

(23) Jana, M. K.; Song, R.; Liu, H.; Khanal, D. R.; Janke, S. M.; Zhao, R.; Liu, C.; Valy Vardeny, Z.; Blum, V.; Mitzi, D. B. Organic-to-inorganic structural chirality transfer in a 2D hybrid perovskite and impact on Rashba-Dresselhaus spin-orbit coupling. *Nat Commun* **2020**, *11* (1), 4699. DOI: 10.1038/s41467-020-18485-7.

(24) Tkatchenko, A.; Scheffler, M. Accurate molecular van der Waals interactions from ground-state electron density and free-atom reference data. *Phys Rev Lett* **2009**, *102* (7),

073005. DOI: 10.1103/PhysRevLett.102.073005.

(25) Perdew, J. P.; Burke, K.; Ernzerhof, M. Generalized Gradient Approximation Made Simple. *PHYSICAL REVIEW LETTERS* **1996**, *77*, 3865-3868.

(26) Liu, C.; Huhn, W.; Du, K. Z.; Vazquez-Mayagoitia, A.; Dirkes, D.; You, W.; Kanai, Y.; Mitzi, D. B.; Blum, V. Tunable Semiconductors: Control over Carrier States and Excitations in Layered Hybrid Organic-Inorganic Perovskites. *Phys Rev Lett* **2018**, *121* (14), 146401. DOI: 10.1103/PhysRevLett.121.146401. Dunlap-Shohl, W. A.; Barraza, E. T.; Barrette, A.; Dovletgeldi, S.; Findik, G.; Dirkes, D. J.; Liu, C.; Jana, M. K.; Blum, V.; You, W.; et al. Tunable internal quantum well alignment in rationally designed oligomer-based perovskite films deposited by resonant infrared matrix-assisted pulsed laser evaporation. *Materials Horizons* **2019**, *6* (8), 1707-1716. DOI: 10.1039/c9mh00366e. Jana, M. K.; Liu, C.; Lidin, S.; Dirkes, D. J.; You, W.; Blum, V.; Mitzi, D. B. Resolving Rotational Stacking Disorder and Electronic Level Alignment in a 2D Oligothiophene-Based Lead Iodide Perovskite. *Chemistry of Materials* **2019**, *31* (20), 8523-8532. DOI: 10.1021/acs.chemmater.9b03208. Jana, M. K.; Janke, S. M.; Dirkes, D. J.; Dovletgeldi, S.; Liu, C.; Qin, X.; Gundogdu, K.; You, W.; Blum, V.; Mitzi, D. B. Direct-Bandgap 2D Silver-Bismuth Iodide Double Perovskite: The Structure-Directing Influence of an Oligothiophene Spacer Cation. *J Am Chem Soc* **2019**, *141* (19), 7955-7964. DOI: 10.1021/jacs.9b02909. Wright, N. E.; Qin, X.; Xu, J.; Kelly, L. L.; Harvey, S. P.; Toney, M. F.; Blum, V.; Stiff-Roberts, A. D. Influence of Annealing and Composition on the Crystal Structure of Mixed-Halide, Ruddlesden–Popper Perovskites. *Chemistry of Materials* **2022**, *34* (7), 3109-3122. DOI: 10.1021/acs.chemmater.1c04213. Lu, H.; Xiao, C.; Song, R.; Li, T.; Maughan, A. E.; Levin, A.; Brunecky, R.; Berry, J. J.; Mitzi, D. B.; Blum, V.; et al. Highly Distorted Chiral Two-Dimensional Tin Iodide Perovskites for Spin Polarized Charge Transport. *J Am Chem Soc* **2020**, *142* (30), 13030-13040. DOI: 10.1021/jacs.0c03899.

(27) Stoumpos, C. C.; Malliakas, C. D.; Peters, J. A.; Liu, Z.; Sebastian, M.; Im, J.; Chasapis, T. C.; Wibowo, A. C.; Chung, D. Y.; Freeman, A. J.; et al. Crystal Growth of the Perovskite Semiconductor CsPbBr3: A New Material for High-Energy Radiation Detection. *Crystal Growth & Design* **2013**, *13* (7), 2722-2727. DOI: 10.1021/cg400645t.

(28) Blum, V.; Gehrke, R.; Hanke, F.; Havu, P.; Havu, V.; Ren, X.; Reuter, K.; Scheffler, M. Ab initio molecular simulations with numeric atom-centered orbitals. *Computer Physics Communications* **2009**, *180* (11), 2175-2196. DOI: https://doi.org/10.1016/j.cpc.2009.06.022.

(29) Huhn, W. P.; Lange, B.; Yu, V. W.-z.; Yoon, M.; Blum, V. GPU acceleration of all-electron electronic structure theory using localized numeric atom-centered basis functions. *Computer Physics Communications* **2020**, *254*. DOI: 10.1016/j.cpc.2020.107314. Yu, V. W.-z.; Moussa, J.; Kůs, P.; Marek, A.; Messmer, P.; Yoon, M.; Lederer, H.; Blum, V. GPU-acceleration of the ELPA2 distributed eigensolver for dense symmetric and hermitian eigenproblems. *Computer Physics Communications* **2021**, *262*. DOI: 10.1016/j.cpc.2020.107808.

(30) Jana, M. K.; Song, R.; Xie, Y.; Zhao, R.; Sercel, P. C.; Blum, V.; Mitzi, D. B. Structural descriptor for enhanced spin-splitting in 2D hybrid perovskites. *Nat Commun* **2021**, *12* (1), 4982. DOI: 10.1038/s41467-021-25149-7.

(31) Huhn, W. P.; Blum, V. One-hundred-three compound band-structure benchmark of post-self-consistent spin-orbit coupling treatments in density functional theory. *Physical Review Materials* **2017**, *1* (3), 033803. DOI: 10.1103/PhysRevMaterials.1.033803.

(32) Yu, V. W.-z.; Campos, C.; Dawson, W.; García, A.; Havu, V.; Hourahine, B.; Huhn, W. P.; Jacquelin, M.; Jia, W.; Keçeli, M.; et al. ELSI — An open infrastructure for electronic structure solvers. *Computer Physics Communications* **2020**, *256*. DOI: 10.1016/j.cpc.2020.107459.

22. Brennan, M. C.; Herr, J. E.; Nguyen-Beck, T. S.; Zinna, J.; Draguta, S.; Rouvimov, S.; Parkhill, J.; Kuno, M., Origin of the Size-Dependent Stokes Shift in $CsPbBr_3$ Perovskite Nanocrystals. *J Am Chem Soc* **2017,** *139* (35), 12201-12208.

23. De Roo, J.; Ibanez, M.; Geiregat, P.; Nedelcu, G.; Walravens, W.; Maes, J.; Martins, J. C.; Van Driessche, I.; Kovalenko, M. V.; Hens, Z., Highly Dynamic Ligand Binding and Light Absorption Coefficient of Cesium Lead Bromide Perovskite Nanocrystals. ACS Nano 2016, 10 (2), 2071-81.

24. Wheeler, L. M.; Sanehira, E. M.; Marshall, A. R.; Schulz, P.; Suri, M.; Anderson, N. C.; Christians, J. A.; Nordlund, D.; Sokaras, D.; Kroll, T.; Harvey, S. P.; Berry, J. J.; Lin, L. Y.; Luther, J. M., Targeted Ligand-Exchange Chemistry on Cesium Lead Halide Perovskite Quantum Dots for High-Efficiency Photovoltaics. *J Am Chem Soc* **2018,** *140* (33), 10504-10513.
25. Safo, I. A.; Dosche, C.; Ozaslan, M., Effects of Capping Agents on the Oxygen Reduction Reaction Activity and Shape Stability of Pt Nanocubes. *Chemphyschem* **2019,** *20* (22), 3010-3023.
26. Ibarra, J.; Melendres, J.; Almada, M.; Burboa, M. G.; Taboada, P.; Juárez, J.; Valdez, M. A., Synthesis and characterization of magnetite/PLGA/chitosan nanoparticles. *Materials Research Express* **2015,** *2* (9), 095010.
27. Li, G.; Huang, J.; Zhu, H.; Li, Y.; Tang, J.X.; Jiang, Y., Surface Ligand Engineering for Near-Unity Quantum Yield Inorganic Halide Perovskite QDs and High-Performance QLEDs. *Chemistry of Materials* 2018, 30 (17), 6099-6107.
28. Jana, M. K.; Song, R.; Liu, H.; Khanal, D. R.; Janke, S. M.; Zhao, R.; Liu, C.; Valy Vardeny, Z.; Blum, V.; Mitzi, D. B., Organic-to-inorganic structural chirality transfer in a 2D hybrid perovskite and impact on Rashba-Dresselhaus spin-orbit coupling. *Nature Communications* **2020,** *11* (1), 4699.
29. Tkatchenko, A.; Scheffler, M., Accurate molecular van der Waals interactions from ground-state electron density and free-atom reference data. *Physical Review Letters* **2009,** *102* (7), 073005.
30. Perdew, J. P.; Burke, K.; Ernzerhof, M., Generalized Gradient Approximation Made Simple. *Physical Review Letters* **1996,** *77*, 3865-3868.
31. Liu, C.; Huhn, W.; Du, K. Z.; Vazquez-Mayagoitia, A.; Dirkes, D.; You, W.; Kanai, Y.; Mitzi, D. B.; Blum, V., Tunable Semiconductors: Control over Carrier States and Excitations in Layered Hybrid Organic-Inorganic Perovskites. *Physical Review Letters* **2018,** *121* (14), 146401.
32. Dunlap-Shohl, W. A.; Barraza, E. T.; Barrette, A.; Dovletgeldi, S.; Findik, G.; Dirkes, D. J.; Liu, C.; Jana, M. K.; Blum, V.; You, W.; Gundogdu, K.; Stiff-Roberts, A. D.; Mitzi, D. B., Tunable internal quantum well alignment in rationally designed oligomer-based perovskite films deposited by resonant infrared matrix-assisted pulsed laser evaporation. *Materials Horizons* **2019,** *6* (8), 1707-1716.
33. Jana, M. K.; Liu, C.; Lidin, S.; Dirkes, D. J.; You, W.; Blum, V.; Mitzi, D. B., Resolving Rotational Stacking Disorder and Electronic Level Alignment in a 2D Oligothiophene-Based Lead Iodide Perovskite. *Chemistry of Materials* **2019,** *31* (20), 8523-8532.
34. Jana, M. K.; Janke, S. M.; Dirkes, D. J.; Dovletgeldi, S.; Liu, C.; Qin, X.; Gundogdu, K.; You, W.; Blum, V.; Mitzi, D. B., Direct-Bandgap 2D Silver-Bismuth Iodide Double Perovskite: The Structure-Directing Influence of an Oligothiophene Spacer Cation. *Journal of the American Chemical Society* **2019,** *141* (19), 7955-7964.
35. Wright, N. E.; Qin, X.; Xu, J.; Kelly, L. L.; Harvey, S. P.; Toney, M. F.; Blum, V.; Stiff-Roberts, A. D., Influence of Annealing and Composition on the Crystal Structure of Mixed-

Halide, Ruddlesden-Popper Perovskites. *Chemistry of Materials* **2022,** *34* (7), 3109-3122.
36. Lu, H.; Xiao, C.; Song, R.; Li, T.; Maughan, A. E.; Levin, A.; Brunecky, R.; Berry, J. J.; Mitzi, D. B.; Blum, V.; Beard, M. C., Highly Distorted Chiral Two-Dimensional Tin Iodide Perovskites for Spin Polarized Charge Transport. *Journal of the American Chemical Society* **2020,** *142* (30), 13030-13040.
37. Stoumpos, C. C.; Malliakas, C. D.; Peters, J. A.; Liu, Z.; Sebastian, M.; Im, J.; Chasapis, T. C.; Wibowo, A. C.; Chung, D. Y.; Freeman, A. J.; Wessels, B. W.; Kanatzidis, M. G., Crystal Growth of the Perovskite Semiconductor $CsPbBr_3$: A New Material for High-Energy Radiation Detection. *Crystal Growth & Design* **2013,** *13* (7), 2722-2727.
38. Blum, V.; Gehrke, R.; Hanke, F.; Havu, P.; Havu, V.; Ren, X.; Reuter, K.; Scheffler, M., Ab initio molecular simulations with numeric atom-centered orbitals. *Computer Physics Communications* **2009,** *180* (11), 2175-2196.
39. Huhn, W. P.; Lange, B.; Yu, V. W.; Yoon, M.; Blum, V., GPU acceleration of all-electron electronic structure theory using localized numeric atom-centered basis functions. *Computer Physics Communications* **2020,** *254*.
40. Yu, V. W.; Moussa, J.; Kůs, P.; Marek, A.; Messmer, P.; Yoon, M.; Lederer, H.; Blum, V., GPU-acceleration of the ELPA2 distributed eigensolver for dense symmetric and hermitian eigenproblems. *Computer Physics Communications* **2021,** *262*.
41. Jana, M. K.; Song, R.; Xie, Y.; Zhao, R.; Sercel, P. C.; Blum, V.; Mitzi, D. B., Structural descriptor for enhanced spin-splitting in 2D hybrid perovskites. *Nature Communications* **2021,** *12* (1), 4982.
42. Huhn, W. P.; Blum, V., One-hundred-three compound band-structure benchmark of post-self-consistent spin-orbit coupling treatments in density functional theory. *Physical Review Materials* **2017,** *1* (3), 033803.
43. Yu, V. W.; Campos, C.; Dawson, W.; García, A.; Havu, V.; Hourahine, B.; Huhn, W. P.; Jacquelin, M.; Jia, W.; Keçeli, M.; Laasner, R.; Li, Y.; Lin, L.; Lu, J.; Moussa, J.; Roman, J. E.; Vázquez-Mayagoitia, Á.; Yang, C.; Blum, V., ELSI — An open infrastructure for electronic structure solvers. *Computer Physics Communications* **2020,** *256*.27.

Table of Content